



Experimental analysis of synthesis process of lanthanum nickelate nanoparticles as an anionic dye adsorbent via a coprecipitation–flux method

| | |
|-------|---|
| メタデータ | 言語: en 出版者: Elsevier © 2021 Elsevier Inc. 公開日: 2022-01-20 キーワード (Ja): キーワード (En): Lanthanum nickel oxide, Coexisting anion, Anionic dye adsorption, Methyl orange 作成者: Iwasaki, Tomohiro, Shimamura, Yasuyuki メールアドレス: 所属: |
| URL | http://hdl.handle.net/10466/00017574 |

Experimental analysis of synthesis process of lanthanum nickelate nanoparticles as an anionic dye adsorbent via a coprecipitation–flux method

Tomohiro Iwasaki*, Yasuyuki Shimamura

Department of Chemical Engineering, Osaka Prefecture University

1-1 Gakuen-cho, Naka-ku, Sakai, Osaka 599-8531, Japan

* Corresponding author. iwasaki@chemeng.osakafu-u.ac.jp

Abstract

Perovskite-type lanthanum nickelate (LaNiO_3) nanoparticles as an adsorbent for removing organic dyes from aqueous solutions were synthesized via a coprecipitation–flux method. In the synthesis process, a mixture of lanthanum hydroxide and nickel hydroxide with sodium nitrate (NaNO_3) as the flux was prepared as the precursor via coprecipitation and heated to promote the LaNiO_3 formation reaction. Various precursors, intermediates and final products were characterized by XRD, FT-IR, FE-SEM, DLS and ICP-OES analyses to investigate the effects of coexisting anions and fluxes in the precursors on the LaNiO_3 formation. When using the precursor with sulfate ions, lanthanum oxide sulfate ($\text{La}_2\text{O}_2\text{SO}_4$) formed as a relatively highly reactive intermediate in the calcination process. This could effectively contribute to the formation of LaNiO_3 at relatively low temperatures. The amount of NaNO_3 flux also affected the purity and particle size of final LaNiO_3 nanoparticles. The adsorption experiments using the LaNiO_3 nanoparticles and anionic dye (methyl orange) as the adsorbent and adsorbate, respectively, demonstrated that the adsorption kinetics and isotherm data were well described by the pseudo-second-order model and the Langmuir model, respectively. The LaNiO_3 nanoparticles had a relatively high adsorption capacity, thereby suggesting that the LaNiO_3 nanoparticles are a promising candidate for the removal of anionic dyes.

Keywords:

Lanthanum nickel oxide, Coexisting anion, Anionic dye adsorption, Methyl orange

1. Introduction

Lanthanum nickelate (LaNiO_3) is a lanthanum-based perovskite-type oxide with excellent properties [1,2]. Several methods for synthesizing LaNiO_3 have been developed so far; in particular, the synthesis of LaNiO_3 nanoparticles with a large surface area and high reactivity has been actively studied in the last decade [3–5]. In many preparation processes, LaNiO_3 nanoparticles can be produced via the solid-phase reaction of a precursor that consists of oxides and/or hydroxides of lanthanum and nickel. To prepare the precursor, various liquid-phase

reaction methods, e.g., sol-gel, hydrothermal and coprecipitation processes, have been employed. However, the conventional solid-phase synthesis methods require relatively long reaction times and/or calcination at high temperatures for the completion of the formation reactions of LaNiO_3 . This may not only increase the process costs and environmental impacts but also decrease the surface area of the resulting LaNiO_3 nanoparticles due to the particle growth during heating.

For reducing the reaction time in the calcination process, a flux method has often been employed [6]. In general, flux methods can promote the chemical reaction and/or crystal growth during the calcination in the liquid-phase environment formed by the melting of the flux component in the precursor. Thus, the flux methods are effective for the synthesis of metal oxide particles within a short time period [7–10]. As a modified flux method, coprecipitation–flux processes have been proposed for the synthesis of complex oxides. In the coprecipitation–flux processes, a precursor that consists of homogeneously and finely mixed reactants is prepared via coprecipitation with liquid-phase reactions and subsequently heated in a flux. The prepared precursor often contains inactive salts (e.g., NaCl , NaNO_3) formed in the coprecipitation process and they can act as a flux. Thus, the reactivity and composition of the precursor plays an important role through the process, which may govern the properties of products. Some studies on the synthesis of LaNiO_3 nanoparticles via coprecipitation–flux processes have been reported [11]. The calcination conditions in the processes, such as calcination atmosphere and temperature, type of fluxes and combination of multiple fluxes, have been examined. However, no investigation has focused on the coprecipitation process for obtaining the precursor that suppresses excessive growth of the LaNiO_3 nanoparticles in the calcination process. For producing LaNiO_3 nanoparticles with smaller sizes and larger surface areas by the coprecipitation–flux processes, the composition of the precursor consisting of reactants and fluxes must be appropriately determined.

LaNiO_3 has been applied to various functional materials: e.g., buffer layers of ferroelectrics [12,13], electrodes of supercapacitor [14], sensing devices [15,16], catalysts for reforming organic compounds [17,18], photocatalysts using visible light-driven photocatalytic activities [3,4,19], etc. As a possible application of LaNiO_3 , adsorbents for removing anionic organic dyes from aqueous solutions have also attracted much attention, because some metal oxides, such as γ -alumina [20], strontium ferrite [21] and cobalt/chromium-codoped zinc oxide [22], exhibit satisfactory dye adsorption properties. It is widely known that adsorption technology is economic feasibility, low toxicity, high effectiveness, environmentally friendliness and simple processing and operation [23]. The LaNiO_3 adsorbents may have not only good adsorption properties but also photocatalytically decompose the organic dyes adsorbed on its surfaces. This may enable to maintain the adsorption performance even in long-term use. In contrast,

conventional adsorbents require posttreatments for recycling such as desorption and thermal treatment to remove the adsorbed dyes. Some researchers have demonstrated that the LaNiO₃ nanoparticles can be a promising candidate as a dye adsorbent for remediation purposes [24–27].

In this paper, we have investigated how the composition of the precursor affects the formation of LaNiO₃ nanoparticles in a coprecipitation–flux process. Namely, the effects of anions and fluxes in the precursor on the solid-phase reaction at relatively low temperatures have been examined, and the formation mechanism is discussed. In addition, using methyl orange which is widely employed as a model adsorbate of anionic organic dye, the adsorption properties have been analyzed based on the kinetics and isotherms.

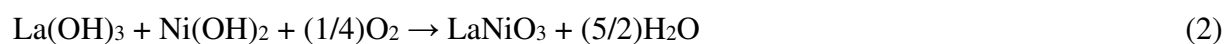
2. Experimental

2.1. Synthesis of LaNiO₃ nanoparticles

All reagents were purchased from FUJIFILM Wako Pure Chemical, except for nickel lactate trihydrate (supplied by Kishida Chemical). They were used in the experiments without further purification. In 25 g of deionized water, 1 mmol of lanthanum nitrate hexahydrate (La(NO₃)₃·6H₂O), 1 mmol of nickel nitrate hexahydrate (Ni(NO₃)₂·6H₂O) and 5 mmol of sodium hydroxide (NaOH) were dissolved. After magnetic stirring for 30 min at room temperature, the suspension was evaporated and dried at 30 °C for 24 h under vacuum. This resulted in formation of a powder mixture as the precursor according to Eq. (1), which consisted of La(OH)₃, Ni(OH)₂ and NaNO₃.



The coexisting anions (e.g., NO₃[−]) in the precursor, which are originated from the raw materials, can affect the solid-phase reaction during calcination [28]. For studying the effects of coexisting anions on the formation of LaNiO₃, instead of Ni(NO₃)₂·6H₂O, nickel chloride hexahydrate (NiCl₂·6H₂O), nickel sulfate hexahydrate (NiSO₄·6H₂O), nickel acetate tetrahydrate (Ni(CH₃COO)₂·4H₂O) and nickel lactate trihydrate (Ni(CH₃CH(OH)COO)₂·3H₂O) were used as the nickel source. The precursors that were prepared using nitrate, chloride, sulfate, acetate and lactate of nickel are denoted as the N-, C-, S-, A- and L-precursors, respectively. The C-, S-, A- and L-precursors contained NaCl, Na₂SO₄, CH₃COONa and (CH₃CH(OH)COO)₂Na, respectively, in addition to NaNO₃. The precursors were calcined at a temperature that ranged from 200 °C and 600 °C for 4 h. The calcination at high temperatures can yield LaNiO₃, according to Eq. (2).



In contrast, the influence of the calcination time longer than 4 h on the phase evolution of the products was relatively small. NaNO₃ in the precursor can act as a flux at temperatures that

exceed its melting point (310 °C) in the calcination process, thereby promoting the crystal growth of the product [6]. After cooling to room temperature, the product was washed by deionized water several times to remove the sodium salts and dried at 110 °C in air for characterization.

In addition, to study the effects of the flux amount in the precursor on the LaNiO₃ formation, a predetermined amount of reagent NaNO₃ was added to the precursor that was prepared with Ni(NO₃)₂·6H₂O and mixed using a mortar and pestle immediately prior to calcination. The addition of NaNO₃ was expressed by the NaNO₃/La(OH)₃ molar ratio in the precursor and varied from 3 (without any addition of NaNO₃) to 12. The NaNO₃-added precursors were calcined at 600 °C, and the products were obtained after washing and drying according to a similar method to that described above.

2.2. Characterization

X-ray diffraction (XRD) analysis was conducted for the precursors, intermediates and final products using a powder X-ray diffractometer (XRD-6100, Shimadzu) with CuK α radiation (30 kV, 30 mA) with a wavelength of 0.154 nm. The average crystallite size of LaNiO₃ in the final products was calculated via the Scherrer equation. The IR spectra of some samples were recorded on an FT-IR spectrometer (IRAffinity-1, Shimadzu) via the diffuse reflectance method. The morphologies of the final products were observed with a field-emission scanning electron microscope (FE-SEM; JSM-6700F, JEOL) at 15 kV. The particle size distribution (number basis) of the final products was measured via dynamic light scattering (DLS; Zetasizer Nano ZS, Malvern). In the measurements, 0.01 g of a final product was added to 20 g of an aqueous solution containing 0.05 mass% cetyltrimethylammonium bromide (CTAB) and 0.05 mass% polyoxyethylene sorbitan monooleate (Tween 80). The resulting suspension was subjected to the particle size analysis after ultrasonication for 10 min using a homogenizer (UH-50, SMT, 50 W, 20 kHz). The contents of La, Ni and Na in the final products were determined via inductively coupled plasma-optical emission spectrophotometry (ICP-OES; SPS7800, SII NanoTechnology). The elemental mapping image of a final product was acquired by a scanning electron microscope–energy dispersive X-ray spectrometry (SEM-EDX; JCM-7000, JEOL).

Using the final product that was prepared from the S-precursor at a NaNO₃/La(OH)₃ molar ratio of 3 as the adsorbent, the kinetics and isotherms for methyl orange (MO) adsorption were examined. MO is a common and typical azo anionic dye used frequently for investigating the adsorption properties of adsorbents. MO was purchased from Kishida Chemical. The adsorption kinetics were investigated via a batch adsorption experiment in which 10 mg of the adsorbent and 10 mL of 100 mg/L MO solution were used. Considering the removal of MO from environmental water, a neutral MO solution was used as the model system. During the

experiments, the adsorbent-added MO solution was maintained at 40 °C under stirring and shaded with a metal cover to minimize the photocatalytic activity. A blank test using adsorbents that the MO adsorption was in equilibrium confirmed that no photocatalytic degradation occurred under shading. After a predetermined contacting time, the supernatant was sampled and immediately filtered to remove the adsorbent. An elemental analysis for the supernatants with EDX confirmed that no toxic metal ions were released from the adsorbents during the adsorption process. The absorbance was measured at a wavelength of 464 nm with a spectrophotometer (V-530, JASCO), and the MO concentration was determined using a calibration curve that had been prepared in advance. The adsorbed amount of MO at a specified time was calculated via Eq. (3).

$$q_t = \frac{(C_0 - C_t)V}{W} \quad (3)$$

where q_t [mg/g] is the adsorbed MO amount at a contacting time t [h], C_0 and C_t [mg/L] are the MO concentrations of the solutions before and after contacting, respectively, V [L] is the volume of the solution, and W [g] is the mass of the adsorbent. Using the data of q_t and t , the adsorption kinetics were analyzed. For analyzing the adsorption isotherms, MO solutions with various initial concentrations that ranged from 50 to 1000 mg/L were used, and similar adsorption experiments to those described above were conducted. The adsorbed amount q_e [mg/g] of MO after contacting for 12 h was determined as an amount of adsorption at equilibrium by substituting the MO concentration C_e [mg/L] at equilibrium for C_t in Eq. (3). Based on the relationship between q_e and C_0 , the adsorption isotherms were investigated.

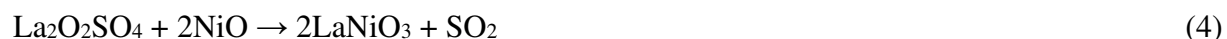
3. Results and discussion

3.1. Effects of coexisting anions in the precursor on LaNiO₃ formation

Fig. 1 presents the XRD patterns of the final products that were obtained from the precursors after calcination at 600 °C. When the A- and L-precursors, which contain organic anions, were used, the products mainly contained NiO, La₂NiO₄ and hexagonal La₂O₂CO₃ (h-La₂O₂CO₃) as the intermediate. This result suggested that the LaNiO₃ formation reaction progressed slowly during calcination, possibly due to the formation of organic metal complexes. In contrast, the N-, C- and S-precursors that contained inorganic anions tended to promote the reaction relatively rapidly compared with the A- and L-precursors. The XRD patterns of the products from the N- and C-precursors showed the peaks indicating small amounts of La₂NiO₄ and NiO together with unknown peaks. However, the use of the S-precursor resulted in the production of LaNiO₃ that contained a tiny amount of intermediates, thereby suggesting that sulfate ions promote the LaNiO₃ formation reaction.

To examine in detail the effects of sulfate ions in the S-precursor on the LaNiO₃ formation,

the S-precursor was calcined at temperatures that were lower than 600 °C, and the intermediates in the obtained samples were analyzed via XRD. Fig. 2 presents the XRD patterns, together with those of the sulfate-ion-free samples that were obtained via calcination of the N-precursor for comparison. From the S-precursor, the product that was obtained at 300 °C contained $\text{La}_2\text{O}_2\text{SO}_4$ in addition to $\text{h-La}_2\text{O}_2\text{CO}_3$, which was not contained in the product from the N-precursor. Furthermore, at 400 °C, the presence of LaNiO_3 was confirmed in the product from the S-precursor but not in that from the N-precursor. This suggested that the subsequent LaNiO_3 formation reaction occurred during the calcination of the S-precursor at relatively low temperatures.



However, at 500 °C, LaNiO_3 was also formed from the N-precursor; hence, $\text{La}_2\text{O}_2\text{CO}_3$ that formed at 400 °C reacted with NiO in both precursors, thereby leading to the formation of LaNiO_3 , according to Eq. (5) [29].



Therefore, the S-precursor can rapidly yield a product that consists of mostly LaNiO_3 , even at relatively low temperatures.

To determine whether the chemical reaction follows Eq. (4), Sw- and Nw-precursors were prepared by washing the S- and N-precursors with deionized water for removing the water-soluble salts (Na_2SO_4 and NaNO_3), respectively. The FT-IR analysis (Fig. 3) confirmed that both the precursors showed absorption bands at approximately 1500, 1390, 1060 and 870 cm^{-1} in the IR spectra, which were attributed to C–O stretching and O–C–O bending vibrations [30–32]. This result suggested that the Sw- and Nw-precursors contained water-insoluble carbonate compounds. Since $\text{La}_2\text{O}_2\text{CO}_3$ formed as the intermediate in the LaNiO_3 formation process from the S- and N-precursors (Fig. 2), the carbonate compound could be LaOHCO_3 that formed in the coprecipitation step via the reaction between $\text{La}(\text{OH})_3$ and CO_2 in air, and intermediate $\text{La}_2\text{O}_2\text{CO}_3$ could form via the decarboxylation of LaOHCO_3 , according to Eqs. (6) and (7) [33].



In addition, the Sw-precursor also had an absorption band at approximately 1100 cm^{-1} , which was due to SO_4^{2-} stretching vibrations [34]. The XRD analysis of the product that was obtained via calcination of the Sw-precursor at 600 °C for 4 h showed that the Sw-precursor that contained no NaNO_3 produced a product that contained not only LaNiO_3 but also $\text{La}_2\text{O}_2\text{SO}_4$ as an unreacted substance after calcination (Fig. 4). The results suggested that $\text{La}_2(\text{OH})_4\text{SO}_4$ formed in the coprecipitation by the reaction between $\text{La}(\text{OH})_3$ and SO_4^{2-} and that the dehydration of $\text{La}_2(\text{OH})_4\text{SO}_4$ yielded $\text{La}_2\text{O}_2\text{SO}_4$ during calcination, according to Eqs. (8) and (9) [35].



Therefore, when using the S-precursor, LaNiO_3 formation may progress relatively rapidly according to Eq. (4), due to the formation of the intermediate $\text{La}_2\text{O}_2\text{SO}_4$ and the presence of the flux NaNO_3 . The proposed formation mechanism will be studied in more detail and described in the next paper.

3.2. Effects of the flux amount on LaNiO_3 formation

According to the XRD analysis (Fig. 5A) of the products that were obtained using the S-precursor at various $\text{NaNO}_3/\text{La}(\text{OH})_3$ molar ratios, larger amounts of intermediates $\text{La}_2\text{O}_2\text{SO}_4$ and h- $\text{La}_2\text{O}_2\text{CO}_3$ remained in the products at higher molar ratios. Increasing the flux amount reduced the concentrations of the reactive components (namely, the lanthanum and nickel species) in the precursor. This can decrease the rate of the LaNiO_3 formation reaction, thereby resulting in remaining the intermediates after calcination. According to the FT-IR analysis (Fig. 5B), the products that were obtained at a molar ratio that exceeded 9 had absorption bands that were due to SO_4^{2-} and CO_3^{2-} , which supported the result of the XRD analysis. Magnified views (Fig. 6) of the XRD patterns for the (101), (110), (202) and (122) planes of LaNiO_3 showed that the diffraction peaks shifted towards higher angles as the flux amount increased. The result suggested that at large flux amounts, La and Ni atoms were substituted with Na atoms, of which the ionic radius is smaller than those of La and Ni. According to the elemental composition (Table 1) that was determined via ICP analysis, the products that were obtained at molar ratios of 3 and 6 had a La/Ni/O molar composition of approximately 1/1/3. A typical EDX mapping image of the product obtained at a molar ratio of 3 (Fig. 7) confirms the LaNiO_3 uniform phase. However, larger flux amounts tended to provide products with relatively low contents of La and Ni. This decreased the purity of LaNiO_3 , which also suggested the substitution of La and Ni atoms with Na atoms.

From the FE-SEM observation (Fig. 8) and the particle size analysis (Fig. 9) of the products, the nanoparticles had diameters of approximately 20–100 nm regardless of the flux amount. The median diameter slightly decreased as the flux amount increased. This may be because the concentrations of reactive species in the melt are lower at large flux amounts, thereby weakening the driving force of mass transfer that is required for the crystal growth [8]. Consequently, the flux amount affected not only the purity of LaNiO_3 in the products but also the particle size, thereby suggesting that it can be used as an operating factor in control of the purity and size of LaNiO_3 nanoparticles.

3.3. Adsorption properties

The amount of adsorbed MO increased as the contacting time elapsed and approximately attained equilibrium in 12 h (Fig. 10). In the IR spectrum of the adsorbent after 24 h (Fig. 11), the adsorption bands were observed at 1120, 1040 and 698 cm^{-1} , which were attributed to the vibrations of the sulfonic group [36–38]. A weak adsorption at 1007 cm^{-1} was attributed to C–H in-plane bending vibration of benzene rings [38]. The results confirmed that the MO molecules adsorbed on the LaNiO_3 nanoparticles.

To investigate the mechanism of adsorption, two kinetic models (namely, pseudo-first-order and pseudo-second-order equation models [39,40]), which are expressed by Eqs. (10) and (11), respectively, were applied to the experimental data (Fig. 12).

$$\ln(q_e - q_t) = \ln q_e - k_1 t \quad (10)$$

$$\frac{t}{q_t} = \frac{1}{k_2 q_e^2} + \frac{t}{q_e} \quad (11)$$

where k_1 [h^{-1}] and k_2 [$\text{g}/(\text{mg}\cdot\text{h})$] are the rate constants of adsorption, q_t [mg/g] is the adsorbed amount at contacting time t [h], and q_e [mg/g] is the equilibrium uptake. The experimental data were more accurately modeled by the pseudo-second-order model than by the pseudo-first-order model, which was similar to the results reported in the literature [24–26]. This suggests that the adsorption of MO by the LaNiO_3 nanoparticles is a chemisorption process which is the rate-determining step [24,26,41–43].

The kinetic results were also analyzed with the intra-particle diffusion model, Eq. (12), to investigate the adsorption behavior in detail.

$$q_t = k_i t^{0.5} + C \quad (12)$$

where k_i [$\text{mg}/(\text{g}\cdot\text{h}^{0.5})$] is the rate constants of intra-particle diffusion and C [mg/g] is a constant [44]. As shown in Fig. 13, the regression line over the whole range of contacting time indicated by the solid line did not fit the kinetic data ($R^2 = 0.654$). However, as shown by the broken line, at an initial stage of the adsorption ($t \leq 3$ h) the plots were almost approximated by a straight line passing through the origin ($R^2 = 0.922$). This suggests that the MO molecules were rapidly transported from the solution to the outside surface of LaNiO_3 nanoparticles at an initial adsorption stage with a relatively high MO concentration.

Subsequently, according to the variation in the equilibrium uptake q_e with the MO concentration C_e at equilibrium at various initial MO concentrations, the adsorption isotherm was analyzed by using the Langmuir model [45] and the Freundlich model [46], which are described by Eqs. (13) and (14), respectively.

$$\frac{C_e}{q_e} = \frac{1}{q_m K_L} + \frac{C_e}{q_m} \quad (13)$$

$$\ln q_e = \ln K_F + \frac{1}{n} \ln C_e \quad (14)$$

where q_m [mg/g] is the maximum adsorption capacity of the adsorbent, K_L [L/mg] is the Langmuir constant, and K_F [L/mg] and n [-] are the Freundlich constants. According to the R^2 values, the Langmuir equation well fitted the experimental adsorption data (Fig. 14), thereby representing a monolayer adsorption on a homogeneous surface. The parameters of kinetic and isotherm models are summarized in Table 2. To investigate in detail the Langmuir isotherm, a dimensionless parameter (separation factor R_L), which was proposed by Hall et al. [47] and is defined by Eq. (15), can be used [41,42].

$$R_L = \frac{1}{1 + K_L C_0} \quad (15)$$

where C_0 is the initial MO concentration. The R_L values for the LaNiO₃ nanoparticles were between 0.041 and 0.461, which were in the range of $0 < R_L < 1$; hence, the LaNiO₃ nanoparticles show satisfactory adsorption of MO under the specified conditions [48]. In addition, R_L was close to zero at high C_0 values, thereby suggesting that the LaNiO₃ nanoparticles undergo an irreversible MO adsorption process at high initial MO concentrations.

The maximum adsorption capacity of the LaNiO₃ nanoparticles was compared with those of various conventional adsorbents (Table 3). Although the adsorption conditions differed among them, the LaNiO₃ nanoparticles had a high level of adsorption capacity similar to that of conventional adsorbents. This resulted in a high adsorption rate and a short equilibrium arrival time, suggesting that the LaNiO₃ nanoparticles can be used for the adsorption of anionic dyes.

The detailed adsorption mechanism including chemisorption will be discussed deeply in another paper, based on the results of adsorption experiments that not only the contacting time and the initial dye concentration but also other conditions such as pH, temperature and adsorbent dosage are widely changed. In addition, the recovery and reuse for recycling of the adsorbents is very important for the practical applications. Furthermore, LaNiO₃ can show a good visible-light-driven photocatalytic activity [4]. Thus, the continuous removal of organic compounds via the synergistic effect of adsorption and photodegradation, i.e., self-regeneration under sunlight, is promising. However, the LaNiO₃ nanoparticles that were synthesized via this method were confirmed to exhibit a very weak photocatalytic activity under visible light, unlike the mechanochemically synthesized LaNiO₃ [4]. The photocatalytic activity must be improved in the future.

4. Conclusions

In the synthesis of LaNiO₃ nanoparticles via a coprecipitation–flux process using the precursor with SO₄²⁻ ions, La₂O₂SO₄, which has a relatively high reactivity, can be formed as an intermediate in the NaNO₃ flux during heating, thereby resulting in the formation of LaNiO₃

at relatively low temperatures. The amount of NaNO_3 flux can also affect the progress of the LaNiO_3 formation reaction, which can be used to control the purity and particle size of the produced LaNiO_3 nanoparticles. The analysis of the kinetics and isotherm of adsorption of an anionic dye MO demonstrated that they obey the pseudo-second-order model and the Langmuir model, respectively, and that the LaNiO_3 nanoparticles possess a relatively high adsorption capacity of 121 mg/g. The results suggest that the LaNiO_3 nanoparticles are a promising candidate for the removal of anionic dye.

References

- [1] A.S. Disa, F.J. Walker, S. Ismail-Beigi, C.H. Ahn, Research update: orbital polarization in LaNiO_3 -based heterostructures, *APL Mater.* 3 (2015) 062303.
- [2] J.A. Dias, M.A.S. Andrade, H.L.S. Santos, M.R. Morelli, L.H. Mascaro, Lanthanum-based perovskites for catalytic oxygen evolution reaction, *ChemElectroChem* 7 (2020) 3173–3192.
- [3] X. Zhou, Y. Chen, C. Li, L. Zhang, X. Zhang, X. Ning, L. Zhan, J. Luo, Construction of LaNiO_3 nanoparticles modified g- C_3N_4 nanosheets for enhancing visible light photocatalytic activity towards tetracycline degradation, *Sep. Purif. Technol.* 211 (2019) 179–188.
- [4] T. Iwasaki, Y. Shimamura, Y. Makino, S. Watano, Mechanochemically assisted synthesis and visible light photocatalytic properties of lanthanum nickel oxide nanoparticles, *Optik* 127 (2016) 9081–9087.
- [5] S. Singh, E. Prestat, L.-F. Huang, J.M. Rondinelli, S.J. Haigh, B.A. Rosen, Role of 2D and 3D defects on the reduction of LaNiO_3 nanoparticles for catalysis, *Sci. Rep.* 7 (2017) 10080.
- [6] E. Mendoza-Mendoza, K.P. Padmasree, S.M. Montemayor, A.F. Fuentes, Molten salts synthesis and electrical properties of Sr- and/or Mg-doped perovskite-type LaAlO_3 powders, *J. Mater. Sci.* 47 (2012) 6076–6085.
- [7] H. Yoshida, L. Zhang, M. Sato, T. Morikawa, T. Kajino, T. Sekito, S. Matsumoto, H. Hirata, Calcium titanate photocatalyst prepared by a flux method for reduction of carbon dioxide with water, *Catal. Today* 251 (2015) 132–139.
- [8] Y. Setsuda, Y. Maruyama, C. Izawa, T. Watanabe, Low-temperature synthesis of BaTaO_2N via the flux method using NaNH_2 , *Chem. Lett.* 46 (2017) 987–989.
- [9] I. Zeydi, A. Zaidi, J. Dhahri, E.K. Hlil, Structural, magnetic and magnetotransport properties of $\text{La}_{0.67}\text{Ba}_{0.332-x}\text{Rb}_x\text{MnO}_3$ perovskites prepared by flux method, *J. Magn. Magn. Mater.* 471 (2019) 529–536.
- [10] J.O. Kroll, J.V. Crum, B.J. Riley, J.J. Neeway, R.M. Asmussen, M. Liezers, Synthesis of $\text{Nd}_3\text{BSi}_2\text{O}_{10}$ using a LiCl -flux method, *J. Nucl. Mater.* 515 (2019) 370–381.
- [11] C.-F. Kao, C.-L. Jeng, Preparation and characterisation of lanthanum nickel strontium oxides by combined coprecipitation and molten salt reactions, *Ceram. Int.*, 26 (2000) 237–243.

- [12] S. Wang, H. Wang, J. Jian, J. Chen, J. Cheng, Effects of LNO buffer layers on electrical properties of BFO-PT thin films on stainless steel substrates, *J. Alloys Compd.* 784 (2019) 231–236.
- [13] J. Zhang, W. Jia, Q. Zhang, J. He, X. Niu, X. Qiao, W. Geng, X. Hou, J. Cho, X. Chou, Controlled spalling and flexible integration of PZT film based on LaNiO₃ buffer layer, *Ceram. Int.* 45 (2019) 6373–6379.
- [14] T. Shao, H. You, Z. Zhai, T. Liu, M. Li, L. Zhang, Hollow spherical LaNiO₃ supercapacitor electrode synthesized by a facile template-free method, *Mater. Lett.* 201 (2017) 122–124.
- [15] J. Parui, B. Murali, B. Biradar, S.B. Krupanidhi, Oxygen deficiency induced nickel based oxides for UV & IR sensitive photo-conductive devices, *Mater. Res. Bull.* 107 (2018) 321–327.
- [16] S. Das, A.S.R. Murthy, K.I. Gnanasekar, V. Jayaraman, Solution processed Mg⁺²:LaNiO₃ thin films for effective methanol sensing, *Sens. Actuators B Chem.* 254 (2018) 526–532.
- [17] Y.W. Cheng, M.R. Khan, K.H. Ng, S. Wongsakulphasatch, C.K. Cheng, Harnessing renewable hydrogen-rich syngas from valorization of palm oil mill effluent (POME) using steam reforming technique, *Renewable Energy* 138 (2019) 1114–1126.
- [18] W.Y. Kim, J.S. Jang, E.C. Ra, K.Y. Kim, E.H. Kim, J.S. Lee, Reduced perovskite LaNiO₃ catalysts modified with Co and Mn for low coke formation in dry reforming of methane, *Appl. Catal. A Gen.* 575 (2019) 198–203.
- [19] T. Lv, M. Wu, M. Guo, Q. Liu, L. Jia, Self-assembly photocatalytic reduction synthesis of graphene-encapsulated LaNiO₃ nanoreactor with high efficiency and stability for photocatalytic water splitting to hydrogen, *Chem. Eng. J.* 356 (2019) 580–591.
- [20] H. Zhang, Y. Ruan, Y. Feng, M. Su, Z. Diao, D. Chen, L. Hou, P.-H. Lee, K. Shih, L. Kong, Solvent-free hydrothermal synthesis of gamma-aluminum oxide nanoparticles with selective adsorption of Congo red, *J. Colloid Interf. Sci.* 536 (2019) 180–188.
- [21] M.Y. Leiw, G.H. Guai, X. Wang, M.S. Tse, C.M. Ng, O.K. Tan, Dark ambient degradation of Bisphenol A and Acid Orange 8 as organic pollutants by perovskite SrFeO_{3-δ} metal oxide, *J. Hazard. Mater.* 260 (2013) 1–8.
- [22] Z. Li, Y. Sun, J. Xing, Y. Xing, A. Meng, One step synthesis of Co/Cr-codoped ZnO nanoparticle with superb adsorption properties for various anionic organic pollutants and its regeneration, *J. Hazard. Mater.* 352 (2018) 204–214.
- [23] Y. Xiang, X. Yang, Z. Xu, W. Hu, Y. Zhou, Z. Wan, Y. Yang, Y. Wei, J. Yang, D.C.W. Tsang, Fabrication of sustainable manganese ferrite modified biochar from vinasse for enhanced adsorption of fluoroquinolone antibiotics: Effects and mechanisms, *Sci. Total Environ.* 709 (2020) 136079.
- [24] S. Farhadi, F. Mahmoudi, Improving the adsorption ability of perovskite-type LaNiO₃ nanomaterial towards organic dyes by hybridizing with phosphotungstic acid, *Polyhedron* 169

(2019) 39–50.

[25] A.G. Santos, J.O. Leite, I.F. Gimenez, M.J.B. Souza, A.M. Garrido Pedrosa, Effect of the B-site cation from LaBO_3 and $\text{LaBO}_3/\text{TiO}_2$ ($\text{B} = \text{Mn}$ or Ni) perovskites prepared by mechanosynthesis in adsorption of Congo red dye from aqueous medium, *Mater. Res. Express* 6 (2019) 105065.

[26] F. Salimi, S. Pire, C. Karami, Eriochrome Black T removal from water solution by modified LaNiO_3 : kinetic, isotherm, and thermodynamic studies, *Desalin. Water Treat.* 179 (2020) 312–322.

[27] Z.N. Garba, W. Zhou, M. Zhang, Z. Yuan, A review on the preparation, characterization and potential application of perovskites as adsorbents for wastewater treatment, *Chemosphere* 244 (2020) 125474.

[28] Y. Fujikawa, F. Yamane, T. Nomura, An effect of anion addition on the reaction rate in the solid state reaction of BaTiO_3 and an analysis of the reaction process, *J. Jpn. Soc. Powder Powder Metall.* 50 (2003) 751–756.

[29] Y. Shimamura, T. Iwasaki, M. Iwata, Analysis of the reaction process in the formation of lanthanum nickel oxide via a mechanochemical route, *Kagaku Kogaku Ronbun.* 44 (2018) 85–90.

[30] S.M. Teleb, M.S. Refat, Synthesis and characterization of lanthanide carbonates obtained during the reaction of urea with lanthanide(III) salts at high temperature, *Bull. Chem. Technol. Macedonia* 25 (2006) 57–60.

[31] J.W. Lee, T. Ahn, D. Soundararajan, J.M. Ko, J. Kim, Non-aqueous approach to the preparation of reduced graphene oxide/ $\alpha\text{-Ni}(\text{OH})_2$ hybrid composites and their high capacitance behavior, *Chem. Commun.* 47 (2011) 6305–6307.

[32] Z. Xu, S. Bian, J. Wang, T. Liu, L. Wang, Y. Gao, Preparation and luminescence of $\text{La}_2\text{O}_3:\text{Ln}^{3+}$ ($\text{Ln}^{3+} = \text{Eu}^{3+}, \text{Tb}^{3+}, \text{Dy}^{3+}, \text{Sm}^{3+}, \text{Er}^{3+}, \text{Ho}^{3+}, \text{Tm}^{3+}, \text{Yb}^{3+}/\text{Er}^{3+}, \text{Yb}^{3+}/\text{Ho}^{3+}$) microspheres, *RSC Adv.* 3 (2013) 1410–1419.

[33] Q. Mu, Y. Wang, Synthesis, characterization, shape-preserved transformation, and optical properties of $\text{La}(\text{OH})_3$, $\text{La}_2\text{O}_2\text{CO}_3$, and La_2O_3 nanorods, *J. Alloy. Compd.* 509 (2011) 396–401.

[34] X. Wang, Y. Du., L. Fan, H. Liu, Y. Hu, Chitosan-metal complexes as antimicrobial agent: synthesis, characterization and structure-activity study, *Polym. Bull.* 55 (2005) 105–113.

[35] X.-Z. Huang, Z. Liu, Y. Yang, Y. Tian, Molten salt synthesis of $\text{La}_2\text{O}_2\text{SO}_4$ nanosheet and their luminescent properties with Eu^{3+} doping, *Funct. Mater. Lett.* 6 (2013) 1350019.

[36] F. Chen, Y. Xie, J. He, J. Zhao, Photo-Fenton degradation of dye in methanolic solution under both UV and visible irradiation, *J. Photochem. Photobiol. A* 138 (2001) 139–146.

[37] Y. Zhang, D. Wang, X. Zhang, F. Qu, Template-free synthesis of porous Cu_2O nanospheres at room temperature and investigation on their adsorption property, *J. Nanomater.* 2013 (2013)

378919.

- [38] P. Zhang, T. Wang, G. Qian, D. Wu, R.L. Frost, Removal of methyl orange from aqueous solutions through adsorption by calcium aluminate hydrates, *J. Colloid Interface Sci.* 426 (2014) 44–47.
- [39] H. Chen, J. Zhao, J. Wu, G. Dai, Isotherm, thermodynamic, kinetics and adsorption mechanism studies of methyl orange by surfactant modified silkworm exuviae, *J. Hazard. Mater.* 192 (2011) 246–254.
- [40] A.A. Jalil, S. Triwahyono, S.H. Adam, N.D. Rahim, M.A.A. Aziz, N.H.H. Hairom, N.A.M. Razali, M.A.Z. Abidin, M.K.A. Mohamadiah, Adsorption of methyl orange from aqueous solution onto calcined Lapindo volcanic mud, *J. Hazard. Mater.* 181 (2010) 755–762.
- [41] V. Vimonses, S. Lei, B. Jin, C.W.K. Chow, C. Saint, Kinetic study and equilibrium isotherm analysis of Congo Red adsorption by clay materials, *Chem. Eng. J.* 148 (2009) 354–364.
- [42] B.H. Hameed, Spent tea leaves: a new non-conventional and low-cost adsorbent for removal of basic dye from aqueous solutions, *J. Hazard. Mater.* 161 (2009) 753–759.
- [43] H. Zaghouane-Boudiaf, M. Boutahala, L. Arab, Removal of methyl orange from aqueous solution by uncalcined and calcined MgNiAl layered double hydroxides (LDHs), *Chem. Eng. J.* 187 (2012) 142–149.
- [44] A.A.A. Darwish, M. Rashad, Hatem A. AL-Aoh, Methyl orange adsorption comparison on nanoparticles: Isotherm, kinetics, and thermodynamic studies, *Dyes Pigm.* 160 (2019) 563–571.
- [45] I. Langmuir, The adsorption of gases on plane surfaces of glass, mica and platinum, *J. Am. Chem. Soc.* 40 (1918) 1361–1403.
- [46] H.M.F. Freundlich, Over the adsorption in solution, *J. Phys. Chem.* 57 (1906) 385–470.
- [47] K.R. Hall, L.C. Eagleton, A. Acrivos, T. Vermeulen, Pore- and solid-diffusion kinetics in fixed-bed adsorption under constant-pattern conditions, *Ind. Eng. Chem. Fundam.* 5 (1966) 212–223.
- [48] S.M.A. El-Gamal, M.S. Amin, M.A. Ahmed, Removal of methyl orange and bromophenol blue dyes from aqueous solution using Sorel's cement nanoparticles, *J. Environ. Chem. Eng.* 3 (2015) 1702–1712.
- [49] T. Jiang, Y.-D. Liang, Y.-J. He, Q. Wang, Activated carbon/NiFe₂O₄ magnetic composite: A magnetic adsorbent for the adsorption of methyl orange, *J. Environ. Chem. Eng.* 3 (2015) 1740–1751.
- [50] Z. Jia, J. Liu, Q. Wang, M. Ye, R. Zhu, Facile preparation of mesoporous nickel oxide microspheres and their adsorption property for methyl orange from aqueous solution, *Mat. Sci. Semicon. Proc.* 26 (2014) 716–725.
- [51] Y. Yao, B. He, F. Xu, X. Chen, Equilibrium and kinetic studies of methyl orange adsorption on multiwalled carbon nanotubes, *Chem. Eng. J.* 170 (2011) 82–89.

- [52] E. Alver, A.Ü. Metin, Anionic dye removal from aqueous solutions using modified zeolite: Adsorption kinetics and isotherm studies, *Chem. Eng. J.* 200–202 (2012) 59–67.
- [53] E.H. Mekatel, S. Amokrane, A. Aid, D. Nibou, M. Trari, Adsorption of methyl orange on nanoparticles of a synthetic zeolite NaA/CuO, *C. R. Chimie* 18 (2015) 336–344.

Table 1Elemental compositions of products that were obtained at various $\text{NaNO}_3/\text{La}(\text{OH})_3$ molar ratios.

| $\text{NaNO}_3/\text{La}(\text{OH})_3$ molar ratio | La [mol.%] | Ni [mol.%] | O [mol.%] | Na [mol.%] |
|---|------------|------------|-----------|------------|
| 3 | 19.1 | 19.7 | 61.2 | 0.0 |
| 6 | 18.3 | 18.9 | 62.8 | 0.0 |
| 9 | 16.1 | 16.6 | 67.2 | 0.1 |
| 12 | 15.3 | 15.9 | 68.6 | 0.2 |

Table 2

Values of the parameters for the adsorption kinetic and isotherm models.

| Model | Parameter | Value |
|-----------------------------------|---|--------|
| Pseudo-first-order kinetic model | q_e [mg/g] | 60.8 |
| | k_1 [h^{-1}] | 0.336 |
| | R^2 | 0.867 |
| Pseudo-second-order kinetic model | q_e [mg/g] | 64.1 |
| | k_2 [$\text{g}/(\text{h}\cdot\text{mg})$] | 0.0132 |
| | R^2 | 0.998 |
| Langmuir isotherm model | q_m [mg/g] | 121 |
| | K_L [L/mg] | 0.0232 |
| | R^2 | 0.998 |
| Freundlich isotherm model | K_F [$\text{mg}/(\text{g}\cdot(\text{mg}/\text{L})^{1/n})$] | 23.1 |
| | n | 4.01 |
| | R^2 | 0.975 |

Table 3Comparison of the maximum adsorption capacities q_m of various adsorbents.

| Adsorbent | Temperature [°C] | pH | q_m [mg/g] | Reference |
|--|---------------------|------------|--------------|-----------|
| LaNiO ₃ nanoparticles | 40 | Neutral | 121 | This work |
| Activated carbon/NiFe ₂ O ₄ composite | 30 | 3 | 182 | [49] |
| Activated carbon | 30 | 3 | 137 | [49] |
| Mesoporous NiO microspheres | 20 | Natural pH | 164 | [50] |
| Multiwalled carbon nanotubes | 60 | 7 | 52.9 | [51] |
| Natural zeolite modified with hexamethylenediamine | 60 | 7 | 58.5 | [52] |
| CuO/NaA zeolite | 25 | 7 | 79.5 | [53] |

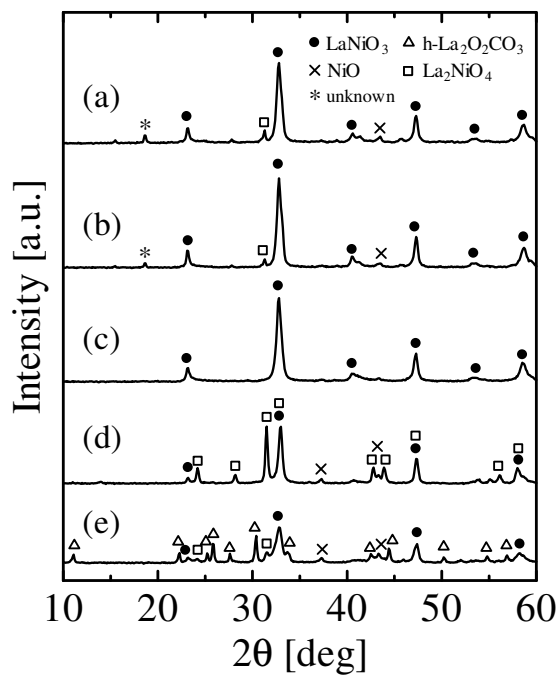


Fig. 1. The XRD patterns of the final products that were obtained after the calcination of (a) N-, (b) C-, (c) S-, (d) A- and (e) L-precursors at 600 °C for 4 h.

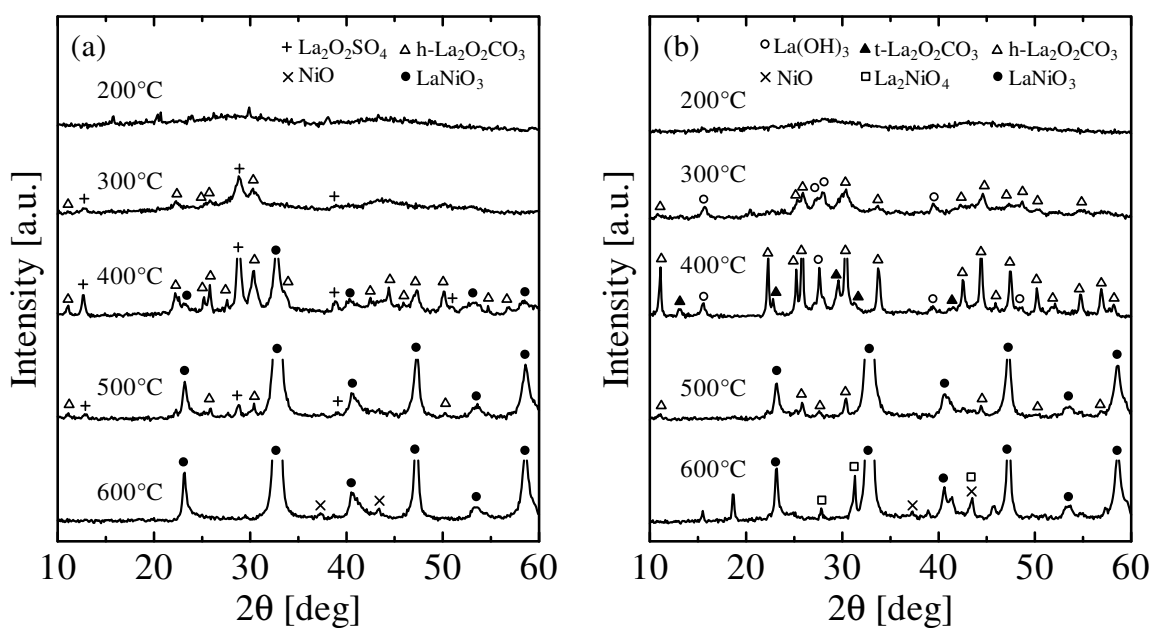


Fig. 2. The XRD patterns of products after calcination of (a) S- and (b) N-precursors at various temperatures for 4 h.

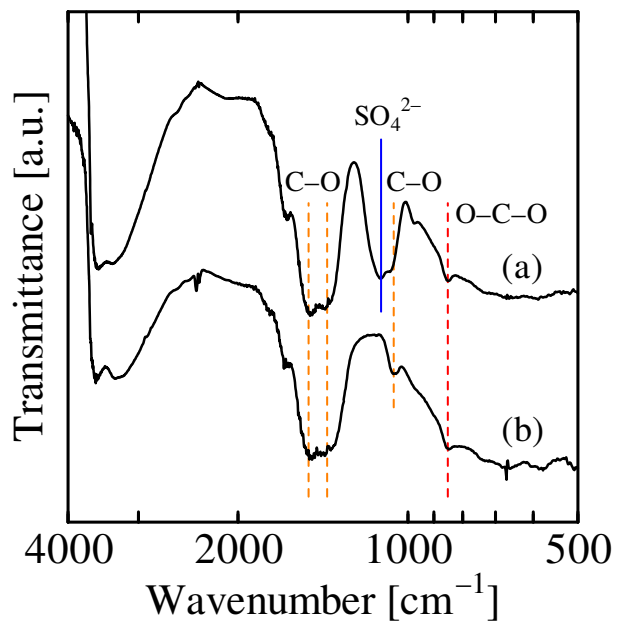


Fig. 3. The FT-IR spectra of the (a) Sw- and (b) Nw-precursors.

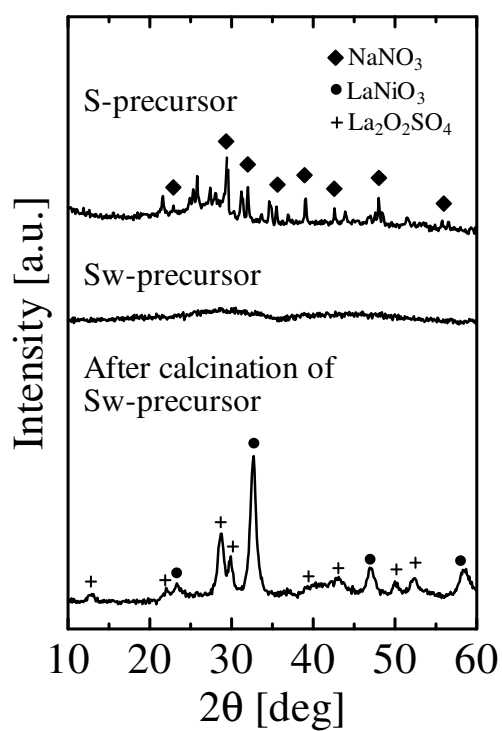


Fig. 4. The XRD patterns of the S- and Sw-precursors and of the final products after calcination of the Sw-precursor at 600 °C for 4 h.

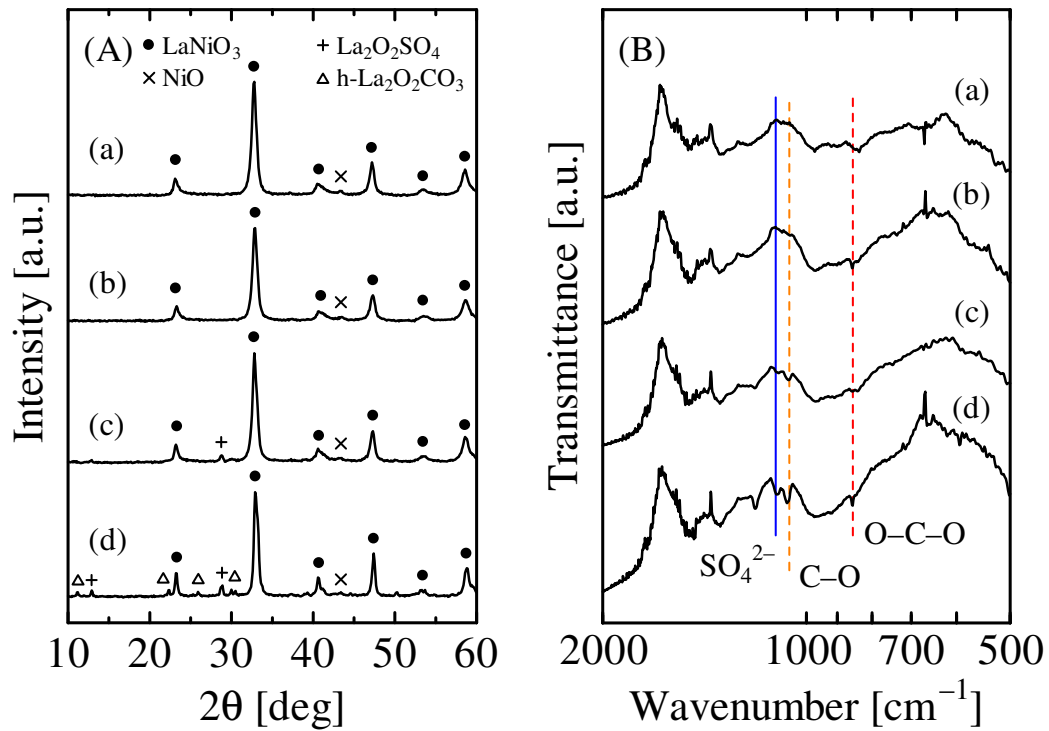


Fig. 5. The (A) XRD patterns and (B) FT-IR spectra of products that were obtained using S-precursor at $\text{NaNO}_3/\text{La}(\text{OH})_3$ molar ratios of (a) 3, (b) 6, (c) 9 and (d) 12.

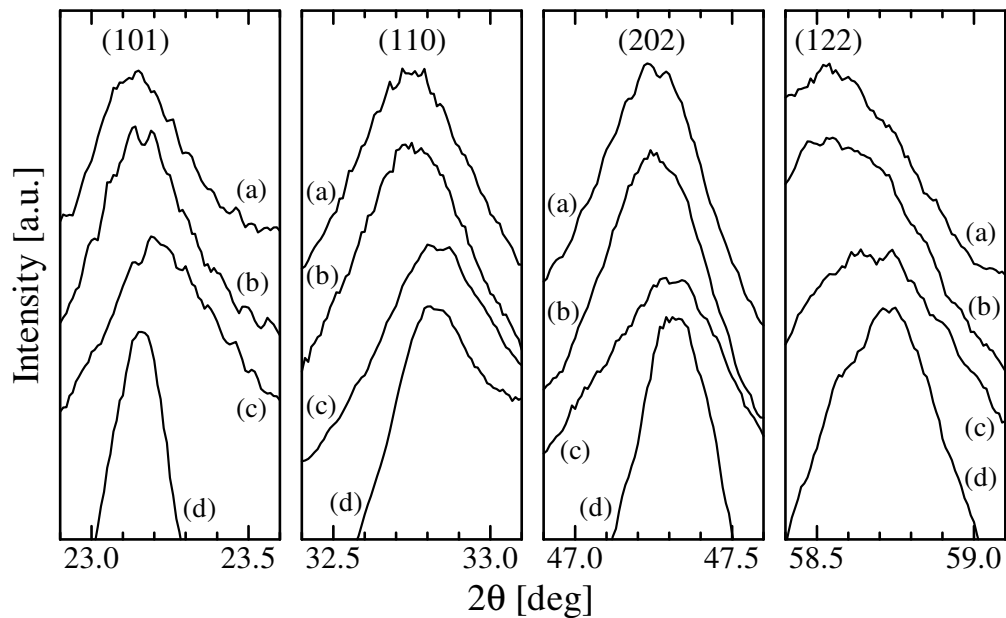


Fig. 6. The magnified XRD patterns of products that were obtained at $\text{NaNO}_3/\text{La}(\text{OH})_3$ molar ratios of (a) 3, (b) 6, (c) 9 and (d) 12.

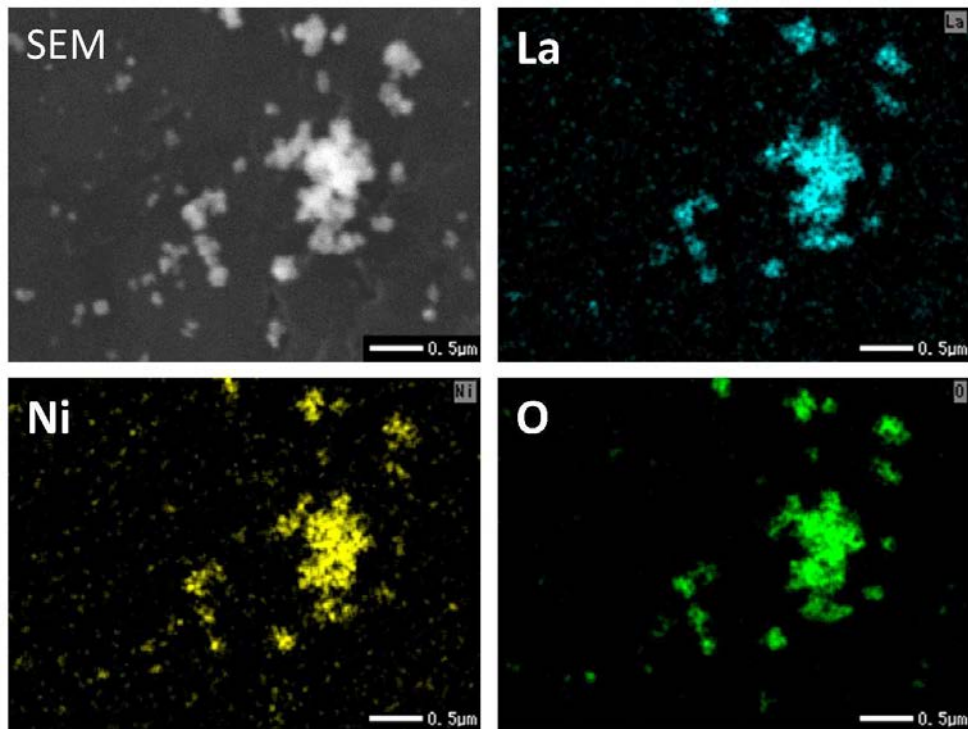


Fig. 7. The typical EDX mapping image of a product obtained at a $\text{NaNO}_3/\text{La}(\text{OH})_3$ molar ratio of 3.

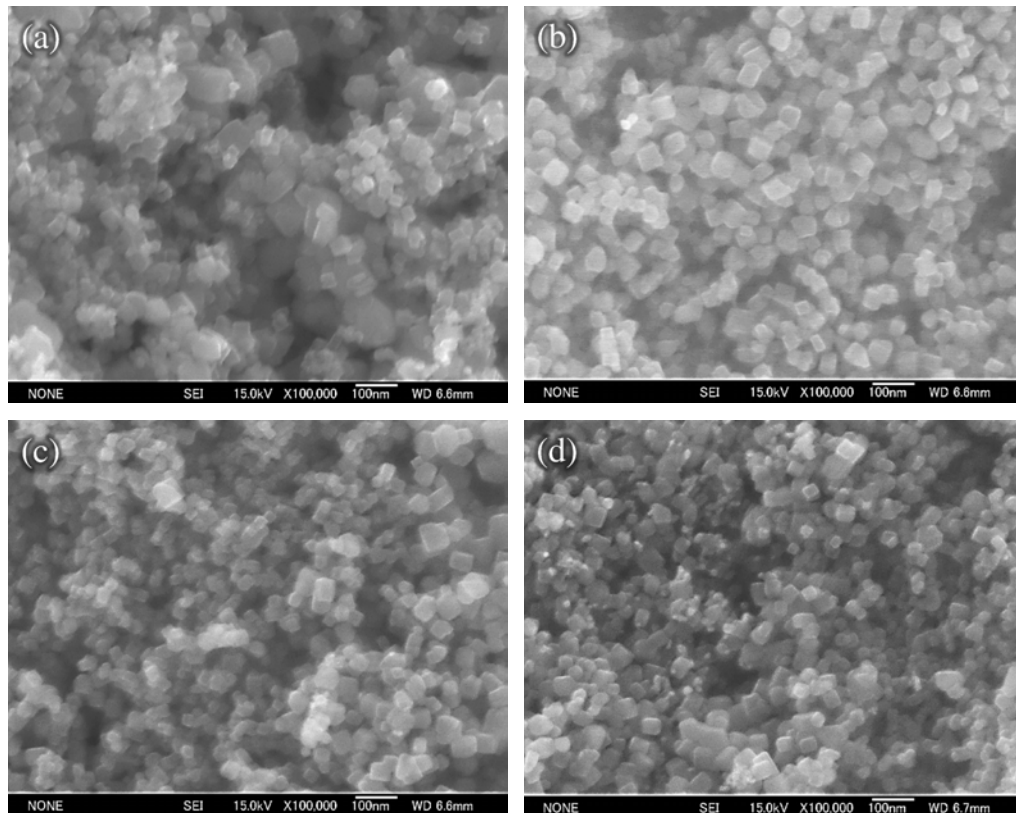


Fig. 8. The typical FE-SEM images of products that were obtained at $\text{NaNO}_3/\text{La}(\text{OH})_3$ molar ratios of (a) 3, (b) 6, (c) 9 and (d) 12.

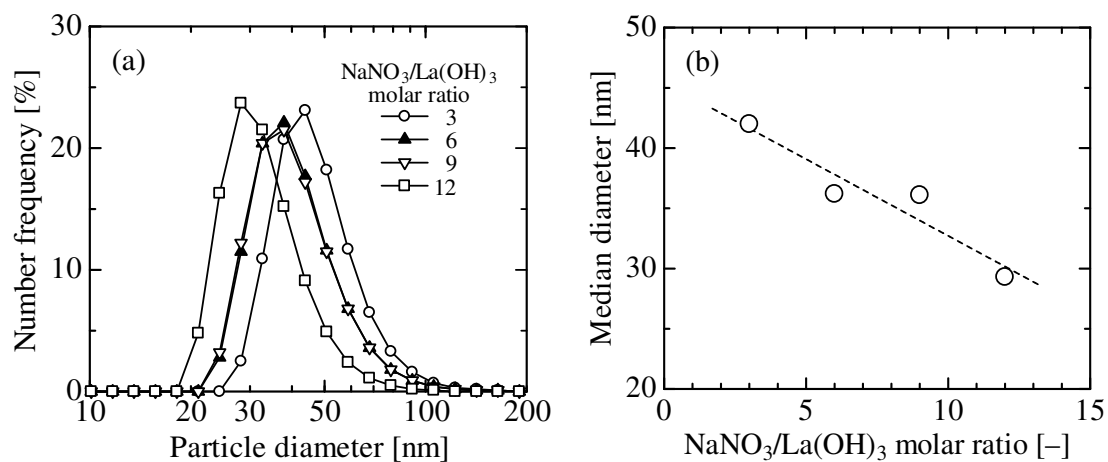


Fig. 9. The (a) particle size distributions and (b) median diameters (number basis) of the final products that were obtained at various NaNO₃/La(OH)₃ molar ratios.

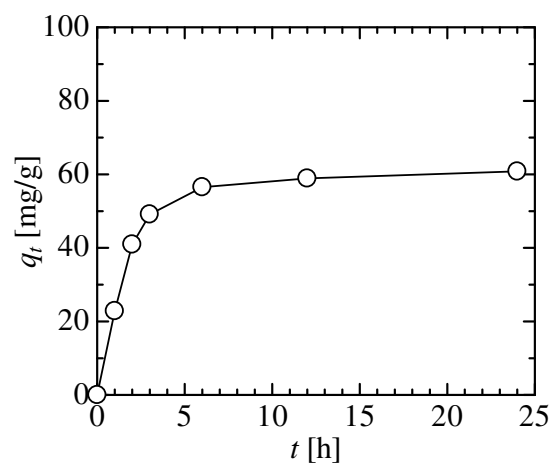


Fig. 10. The MO adsorption as a function of the contacting time ($C_0 = 100$ mg/L).

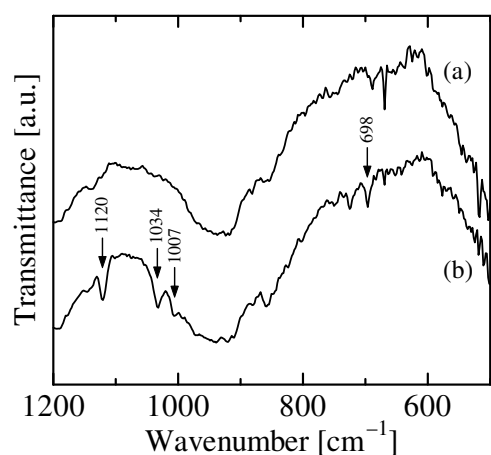


Fig. 11. The FT-IR spectra of LaNiO₃ nanoparticles (a) before and (b) after MO adsorption for 24 h.

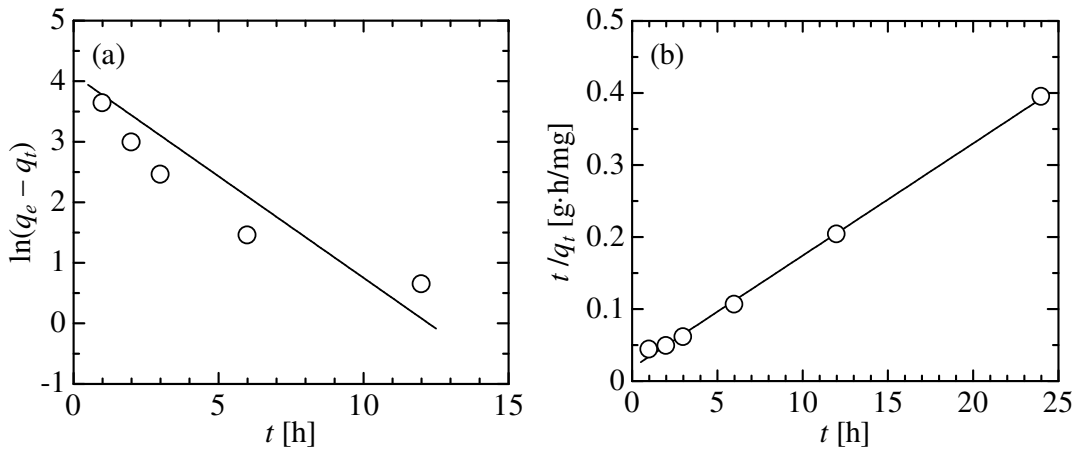


Fig. 12. The adsorption kinetics of LaNiO₃ nanoparticles: (a) pseudo-first-order ($q_e = q_t$ at $t = 24$ h) and (b) pseudo-second-order plots ($C_0 = 100$ mg/L).

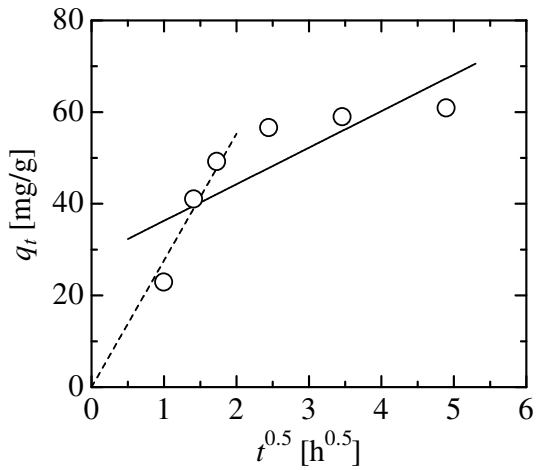


Fig. 13. The intra-particle diffusion plots for adsorption of MO onto LaNiO₃ nanoparticles.

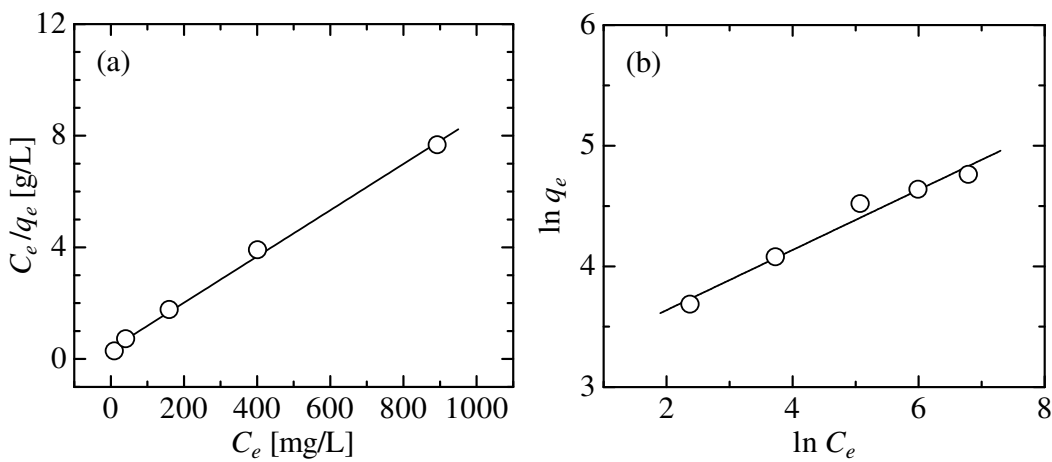


Fig. 14. The (a) Langmuir and (b) Freundlich plots for adsorption of MO onto LaNiO₃ nanoparticles.